Chemical Engineering Journal 469 (2023) 143942

Contents lists available at ScienceDirect

Chemical Engineering Journal

journal homepage: www.elsevier.com/locate/cej

High-entropy transition metal disulfide colloid clusters: synergistic atomic scale interaction and interconnected network for ultra-stable potassium ion storage

Yan-Jie Liao, Wei-Wen Shen, Che-Bin Chang, Hsing-Yu Tuan *

Department of Chemical Engineering, National Tsing Hua University, Hsinchu 30013, Taiwan

ARTICLE INFO

Keywords:
Potassium ion battery
Metal chalcogenide
Anode
Clusters
High entropy

ABSTRACT

High-entropy metal disulfide (HES_2) colloid clusters were synthesized through a two-step templated solvothermal method for used as anode materials for potassium-ion storage devices. HES_2's large configuration entropy stabilizes its crystal structure and promotes chemical diversity by introducing multiple cations, thus reducing the impact of the shuttle effect, retaining active materials and extending cycling life up to 1800 cycles. During cycling, crystalline-amorphous grain boundaries formed in situ enhance electrochemical reaction activities and ensure the exposure of active sites. Elements with lower electronegativity allow S to bring more negative charges, improving the electrostatic force between S and K^+ and enabling better anchoring of potassium polysulfide. Meanwhile, the retained close-packed cluster structure of HES_2 provides a large contact area to accelerate the reduction reaction of the electrolyte in the sphere during the repeating K^+ insertion/extraction. We further demonstrate the excellent performance of HES_2 anodes on practical potassium-ion full battery and hybrid capacitor applications. The pioneering concept in atomic compositional engineering and structural design of transition metal sulfide electrodes presented in this work marks a significant step forward in the development of chalcogenide electrode systems for energy storage devices.

1. Introduction

Lithium-ion batteries (LIBs) are primarily used in electronic devices from their long cycle life, high energy density, and excellent rate performance [1–3]. However, with increasing demand for electric vehicles and energy storage grids, the scarcity (0.0017 %) and uneven distribution of lithium metal (with 70 % in South America) has led to rising costs [4,5]. Potassium-ion batteries (PIBs) are considered a promising alternative for their abundant and uniform distribution of potassium metal (1.5 %) in the earth's crust [6]. The weaker Lewis acidity makes potassium ions with a smaller ionic radius after solvation, increasing their conductivity and transportation ability [7]. The lower desolvation energy enhances the diffusion between the electrolyte and electrode interface [8,9]. PIBs electrode materials can be classified into intercalation compounds, carbonaceous materials, alloy materials, and conversion materials based on K^+ reaction behavior. However, the development of PIBs is hindered by its relatively large atomic radius of potassium ions (K^+: 0.138 nm; Li^+: 0.076 nm), causing severe volume expansion and decreasing storage capacity [10,11].

Transition metal sulfides (TMS) have been explored as potential conversion anodes for PIBs due to their ability to undergo a multiple electron transfer reaction by converting K_2S. Each S^{2-} can store two electrons to provide a high theoretical capacity. Additionally, K_2S has a higher conductivity than K_2O [12]. The weaker M−S bond in TMS compared to M−O results in a relatively kinetically favorable conversion reaction [13]. Despite having faster potassium ion reaction kinetics [14], current TMS anodes still face challenges. Polysulfides, such as K_2S, K_2S_2, and K_2S_3, dissolve in the electrolyte causing the shuttle effect, and the structural instability caused by the conversion reaction leads to volume expansion and eventually causes deactivation. Recent studies have focused on addressing the challenges of ionic diffusion distance and volume expansion by constructing nanoscale structures [15,16]. For instance, FeS_2@C with a core–shell structure is uniformly encapsulated in 3D hollow carbon spheres, with the graphene shell acting as a pocket to prevent polysulfides from losing during the redox process [17]. In the case of CoS_2-CNs, each nanocarbon shell can confine a single nanoparticle, preventing serious aggregation during the reaction [18]. Additionally, synthesizing different crystal structures of nickel sulfide

* Corresponding author.
E-mail address: hytuan@che.nthu.edu.tw (H.-Y. Tuan).

https://doi.org/10.1016/j.cej.2023.143942
Received 15 March 2023; Received in revised form 14 May 2023; Accepted 3 June 2023
Available online 5 June 2023

can relieve more stress due to its hexagonal structure [13]. The volume expansion of CuS is reduced by a protective shell layer, resulting in a more stable SEI layer [19]. However, problems such as structural degradation and the shuttle effect of polysulfides still need to be overcome to develop a high-performance and stable anode.

High-entropy metal sulfides (HESs) are a class of high-entropy materials (HEMs) that have been discovered in recent years [20]. The concept of high entropy involves introducing multiple major elements into single-phase lattices, as first proposed by Yeh [21]. High-entropy alloys have three key characteristics that are relevant to high-entropy metal sulfides (HESs): the high-entropy effect, the lattice distortion effect, and the cocktail effect. The high-entropy effect pertains to the material's stabilization ability in a single-lattice phase, while lattice distortion effects are caused by substituting various sizes of cations in a single lattice. Finally, the cocktail effect is to describe any unexpected properties that cannot be explained by any single element [22]. This effect has recently attracted the interest of catalysis researchers, as in the case of $(CrMnFeCoNi)S_x$ solid solution nanoparticles, which show synergy between metal atoms and are used in the oxygen evolution reaction (OER) [23–25]. Additionally, the lattice distortion effect has been observed in the thermoelectric material, such as the thermal conductivity of $Pb_{0.89}Sb_{0.012}Sn_{0.1}Se_{0.5}Te_{0.25}S_{0.25}$ has been significantly reduced [26]. Despite these promising effects, high-entropy alloy sulfides are still infrequently used as materials for energy storage batteries. Recently, high-entropy MS_2 prepared by the mechanical alloying method exhibited better battery performance than low-entropy CoS_2, suggesting the contribution of the cocktail effect [21]. Furthermore, the application of the $Cu_4MnFeSnGeS_8$ high-entropy configuration to Na-ion batteries represents an example of the high-entropy effect in action. This configuration's mechanical stability effectively relieves the accumulated stress and inhibits the continuous rupture of the SEI film, leading to an improvement in cycle performance (5 A g^{-1}, 1200 cycles) [27].

Herein, TMS electrodes for potassium ion storage devices were introduced the design strategy of high entropy chalcogenides for the first time. We report a high-entropy transition metal disulfide (HES_2) spheres composed of clusters obtained from sulfurization of a high-entropy glycerate sphere templates. As shown in Scheme 1, the clusters possess effective transport paths for potassium ions and a highly conductive network, making them more suitable for the insertion/extraction of K^+ without losing inter-cluster contact, thereby enabling ultralong cycling performance. Additionally, the in-situ formation of numerous crystalline-amorphous grain boundaries promotes electrochemical reaction activities, ensuring the exposure of active sites. After potassiation, the formed high-entropy alloys exhibit a strong anchoring effect of polysulfides. The HES_2 anode exhibits excellent electrochemical performance, maintaining exceptional stability at 348 mA h g^{-1} after 1800 cycles at a current density of 500 mA g^{-1}. Furthermore, for full cells and hybrid capacitors, it shows a capacity of 258.6 mA h g^{-1} after 1000 cycles and an energy density of 63.7 Wh kg^{-1} after 6000 cycles, respectively.

2. Results and discussion

A simple solvothermal method was employed to prepare uniform high entropy glycerate (HEG) template spheres as precursors having an average diameter about 600 nm (Figure S1), which were then converted to colloidal HES_2 clusters via a sulfidation process. The formation process was elucidated through the decomposition of thiourea at high temperature. The released sulfide (S^{2-}) ions subsequently reacted with the metal oxides on the surface of HEG. This reaction can be described as an anion exchange reaction of HEG (Fig. 1a). In order to illustrate the formation mechanism of high entropy metal disulfide nanospheres, studies were performed using scanning electron microscopy (SEM) and transmission electron microscopy (TEM) to monitor the morphological evolution as a function of sulfurization time. The surface of HEG was observed to be smooth without visible pores (Fig. 1(b), (f) and Figure S2 (a)). After sulfurization treatment at 160 °C for approximately 0.5 h, the color changed from a dark yellow to black color, indicating the formation of metal sulfides. The product remained a solid sphere, but the surface became slightly rougher, owing to the sulfurization reaction on the surface. (Fig. 1(c), (g) and Figure S2(b). With an extended reaction time of 6 h, more cluster sulfides were formed and made the surface becomes rougher (Fig. 1(d), (h) and Figure S2(c)). The reaction time was further increased to 8 h to completely sulfurize the template into the colloidal HES_2 (Fig. 1(e), (i) and Figure S2(d)), where these solid nanospheres were composed of stacked clusters. The SEM image in Fig. 1 (j) shows multiple nanospheres. HRTEM images in Fig. 1(k) and (l) show lattice fringes of 0.319 nm correspond to the (111) plane of the CoS_2(PDF#00–041-1471). The selected area electron diffraction (SAED) pattern (Fig. 1m) shows five ring patterns corresponding to (111), (200), (210), (220) and (311) crystal planes of cubic CoS_2 with Pa-3 space group, consistent with the XRD peaks located at 28°, 32°, 36°,

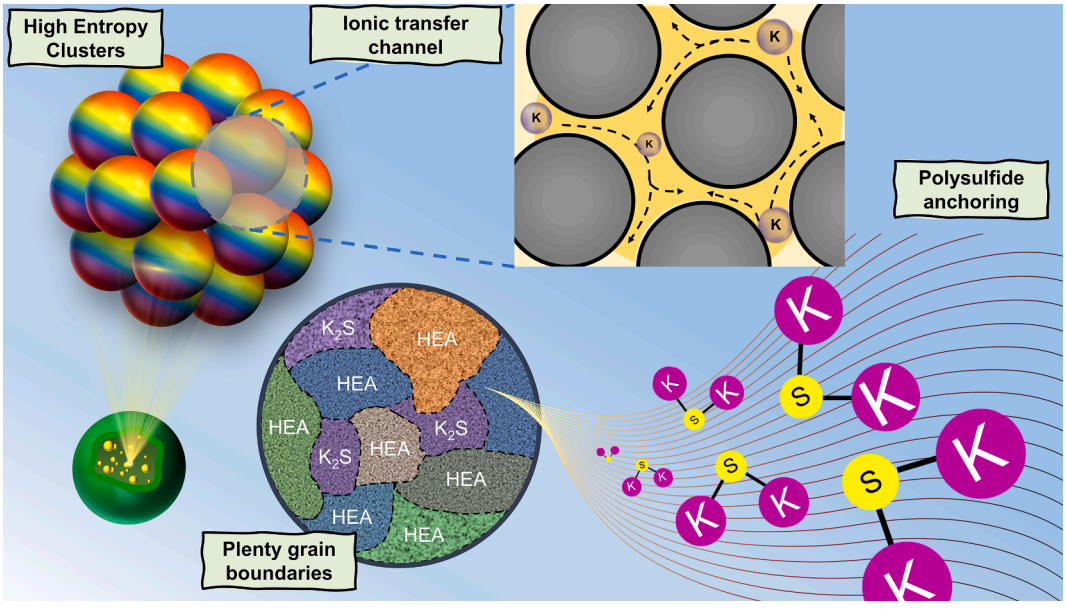

Scheme 1. High entropy clusters with ionic transfer channel and plenty grain boundaries have a strong affinity to polysulfides, inhibiting the shuttle effect.

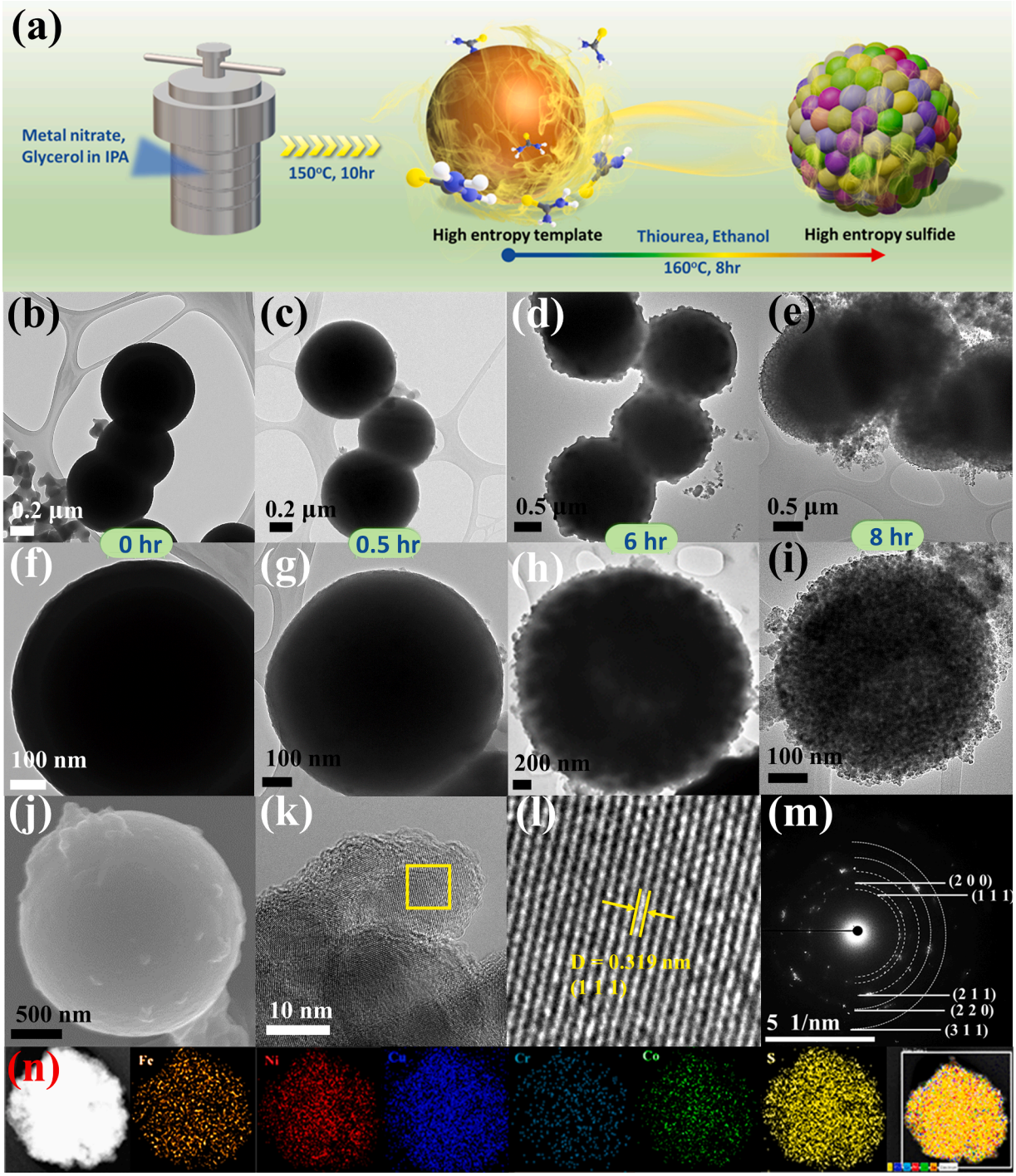

Fig. 1. (a) Schematic illustration of synthesis process of HES_2. (b, f) High entropy glycerate spheres and products obtained after sulfurization of high entropy glycerate at 160 °C at different times: (c, g) 0.5 h; (d, h) 6 h; (e, i) 8 h. (j) SEM image of HES_2. (k, l) high resolution TEM images. (m) SAED pattern. (n) EDS element mapping.

45°, 55°. TEM-EDS indicates even elemental distribution at the nanometer scale, without any obvious accumulation or segregation of individual elements. The content of each element roughly corresponded to the stoichiometric atom ratio, and is consistent with ICP- MS results. Additional detailed morphology and microstructural information for MES_2 and CoS_2 samples can be found in the supporting information Figure S3-S6. In the case of HES_2 with graphite, XRD, SEM, TEM, Raman and BET were shown in Supporting Information Figure S7-11. Finally, the weight contents of HES_2 were determined by thermogravimetric analysis (TGA), indicating a value of approximately 71 wt % (Figure S12 Supporting Information). The XRD pattern of HES_2 after TGA measurement is supplied in the supporting information (Figure S13).

Fig. 2(a) displays the X-ray diffraction (XRD) patterns of four types of metal disulfides clusters through two-step solvothermal sulfurization. The XRD pattern of HEG was shown in Figure S14. All the samples possess a cubic pyrite metal sulfide structure (PDF#00-041-1471) with the space group Pa-3. The high entropy metal disulfide $(FeCoNiCuCr)S_2$ is labeled as HES_2, while the medium entropy metal disulfide $(FeCoNiCu)S_2$ is referred to as MES_2. The sample containing impurity phases ($Cu_{7.2}S_4$, $(Fe_{0.11}Co_{0.8}Ni_{0.09})S_2$, $(Co_{0.85}Cr_{0.15})S_2$, Co_3S_4 and Ni_3S_2) is

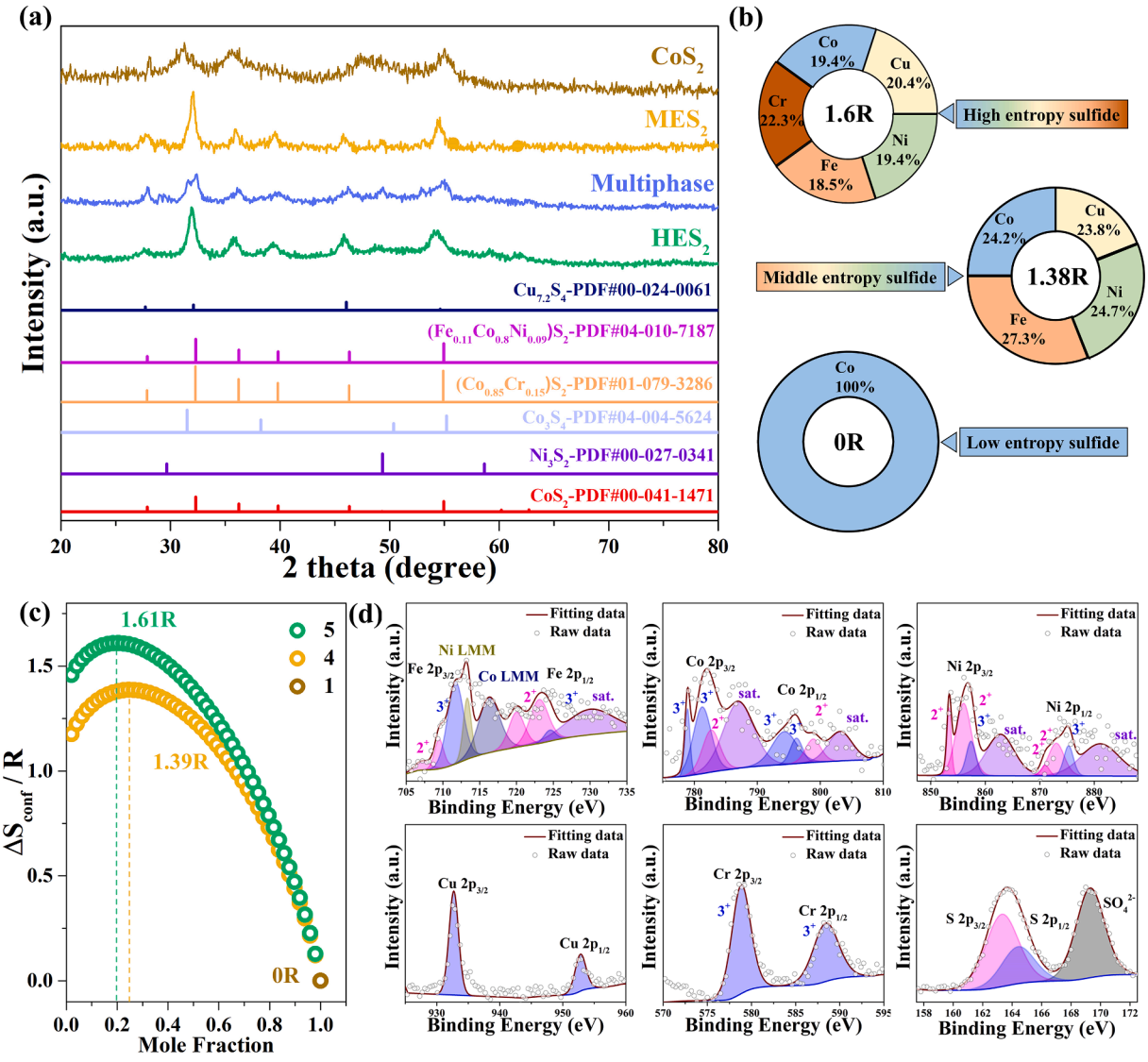

Fig. 2. (a) XRD patterns of HES_2, MES_2, CoS_2 and multiphase. (b) Stoichiometry of HES_2, MES_2, CoS_2 from ICP-MS analysis. (c) Dependence of configurational entropy on the number of elements. (d) High-resolution XPS spectra of Fe, Co, Ni, Cu, Cr, S.

marked as multiphase. Normally, the only phase present in the sample is the cubic pyrite metal sulfide. The crystal structure and morphology have changed after sulfurization, the smooth surface of glycerate templates becoming cluster sulfides (Figure S2(d)) (Supporting Information). Powder X-ray diffraction (XRD) analysis showed the formation of single-phase HES_2 sample, and the main diffraction peaks were located at 28°, 32°, 36°, 40°, 45°, and 55°. The crystal structure of the HES_2 model was refined on powder X-ray diffraction (XRD), and the corresponding Rietveld refinement profiles were shown in Figure S15(a, b) (Supporting Information). The lattice parameters of three materials in the supporting information Table S1 showing the lattice has stretched caused by the introduction of multi-cations. The materials HES_2 and MES_2 underwent different degrees of stretching with HES_2 having the highest degree at 1.3 %, followed by MES_2 at 0.632 %, and both stretching more than CoS_2.The experimental and simulated XRD patterns reach mutual corroboration verifies the successfully synthesis of HES_2 and MES_2 clusters. To determine the ratio of multi-cations in the individual samples, inductively coupled plasma-mass spectrometry (ICP-MS) are used and listed in Fig. 2(b). All samples have almost equimolar metals. The configurational of high entropy system (ΔS_{conf}) was calculated to be 1.61R (Fig. 2(c)) by using the statistical thermodynamics derived from the definition of ΔS_{conf} (equations (S1) and (S2)) in the Supporting Information. Because the increase in the configuration entropy is greater than the enthalpy, the crystal structure can be stabilized. Compared with HES_2, the ΔS_{conf} of MES_2 was decreased to 1.39R (0.25 mol each) after removing a cation [28]. X-ray photoelectron spectroscopy (XPS) was conducted to comprehend the valence states of the HES_2 sample. Fig. 2(d) shows that in the Fe 2p spectrum, the peaks near 707.2 and 709.6 eV belong to Fe $2p_{3/2}$ (Fe^{2+}) [29]. The peak around 723 eV is attributed to Fe $2p_{1/2}$ (Fe^{2+}). Peaks near 711.6 eV (Fe $2p_{3/2}$) and 724.4 (Fe $2p_{1/2}$) eV correspond to Fe^{3+}. Three satellite peaks are seen 715.5, 718.3 and 730.2 eV. Notably, Ni LMM and Co LMM are overlapped with the Fe 2p spectrum, 713.0 eV and 716.0 eV, respectively [30,31]. In Ni 2p spectra, there are three peaks at 853.4 and 865.1 eV (Ni $2p_{3/2}$) and 870.9 eV (Ni $2p_{1/2}$) of Ni^{2+}. Peaks at 857.3 (Ni $2p_{3/2}$) and 875.2 eV (Ni $2p_{1/2}$) are attributed to Ni^{3+}, while there are two satellite peaks near 862.7 and 881.5 eV [32]. In the Co 2p spectrum, Co $2p_{3/2}$ (Co^{3+}) are further deconvoluted into two peaks at 778.9 and 781.3 eV. Two peaks located at 778.9 and 794.2 eV can be ascribed to Co $2p_{1/2}$ (Co^{3+}). The Co $2p_{3/2}$ (Co^{2+}) and Co $2p_{1/2}$ (Co^{2+}) peaks are found at 782.6 and 798.9 eV, respectively. The peaks at 786.9 and 803.6 eV are satellite peaks [33]. In the Cr 2p spectrum, two sharp peaks of the single valence state (Cr^{3+}) were found, located at 577.8 and 587.4 eV, corresponding to Cr $2p_{3/2}$ and Cr $2p_{1/2}$, respectively [34]. In the high

resolution XPS for Cu, there are two strong peaks, Cu $2p_{3/2}$ at 932.5 eV and Cu $2p_{1/2}$ at 952.2 eV, corresponding to Cu^{1+} [35]. It is worth noting that the S 2p peaks at 162.7 (S $2p_{3/2}$) and 163.9 eV (S $2p_{1/2}$) correspond to S^{2-} of metal disulfides; the peak at 169.2 eV belongs to sulfate component (SO_4^{2-}). The strong peak of SO_4^{2-} supports the above mentioned of sulfate formation. These XPS result showing high consistence with Nguyen et al. reported on HES_2, indicating the formation of HES_2 [36].

After the successful introduction of high entropy configuration confirmed by structural and chemical characterizations, it is considerable to study the relationship between electrochemical properties and high entropy configurations. To further investigate the evolution of cycling performance, the half cells of all samples were measured at a current density of 0.05 A g^{-1} for the initial three cycles. The reaction plateaus of the discharge–charge curves of all samples were consistent with the corresponding CV curves (Fig. 3(a)-(d)). The HES_2 electrode provided the discharge and charge capacity of 719.9 and 403.36 mA h g^{-1} with 56.1 % initial coulombic efficiency (ICE). The CoS_2 electrode provided the discharge/charge capacity of 598.8 and 442.3 mA h g^{-1}. (ICE of 73.7 %). The multiphase electrode provided the discharge/charge capacity of 739.7 and 479.9 mA h g^{-1} with an ICE of 64.8 %. The MES_2 electrode provided the discharge/charge capacity of 839.2 and 416.7 mA h g^{-1} with an ICE of 49.7 %. The lower ICE indicates the SEI layer formed and irreversible potassium loss during the initial cycle. Subsequently, the discharge–charge curves of HES_2 overlapped, indicating its high conversion consistency and reversibility. However, compared to other electrodes (MES_2, CoS_2, and multiphase), there is a capacity loss in the following cycles. At low current density of 0.05 A g^{-1}, the HES_2 electrode maintained the discharge capacity of 474.2 mA h g^{-1} for 350th cycle, representing an outstanding electrochemical cycling stability. (Fig. 3e) To further investigate the kinetics analysis of potassium ions, the rate capabilities of four sulfide electrodes were tested at various current densities ranging from 0.5 to 5 A g^{-1}. The HES_2 electrode exhibited almost the best discharge capabilities and the highest energy densities at all current densities (Fig. 3f, g). Specifically, it delivers 396.6, 334.7, 276, 237.3, 199.2, 162.3, 135.9, and 105.3 mA h g^{-1} at increasing current densities from 0.05, 0.1, 0.2, 0.5, 1.0, 2.0, 3.0 to 5.0 A g^{-1}, respectively (Fig. 3f). Notably, the initial capacity of MES_2 is due to unstable conversion reaction of polysulfides and the repeated SEI layer formation caused by the cracking of the MES_2 electrode. Therefore, MES_2 exhibited a higher capacity at the initial cycle number [37]. Such an outstanding rate capability indicates the superior kinetic movement of potassium ions in the high entropy configuration. In addition, the discharge capacity of HES_2 can still be maintained at 457.7 mA h g^{-1} as return to 0.05 A g^{-1}, demonstrating its excellent structural and electrochemical stability after undergoing severe tests of high current densities. In contrast, other electrodes of non-high entropy configurations show poor rate performances and stabilities due to structural disruption and degradation of reaction kinetics during repeated and fast (de)potassiation processes. The capacity of multiphase half-cell faded significantly after 150 cycles. The battery provided discharge and charge capacities of 42.16 and 41.6 mA h g^{-1} at the 150^{th} cycle, and finally returned to zero capacity at the 200^{th} cycle. Interestingly, this issue was slowly suppressed with the increase of ΔS_{conf}. For the CoS_2 half-cell, the capacities also faded after 150 cycles. The battery provided discharge and charge capacities of 96.9 and 96.1 mA h g^{-1} at 150 cycles, which is almost twice the capacity of the multiphase electrode. The battery finally had discharge and charge capacities of 86.2 and 85.6 mA h g^{-1} at the 300^{th} cycle. For the MES_2 half-cell ($\Delta S_{conf} = 1.39$ R), the capacities faded slightly after 150 cycles. The battery provided discharge and

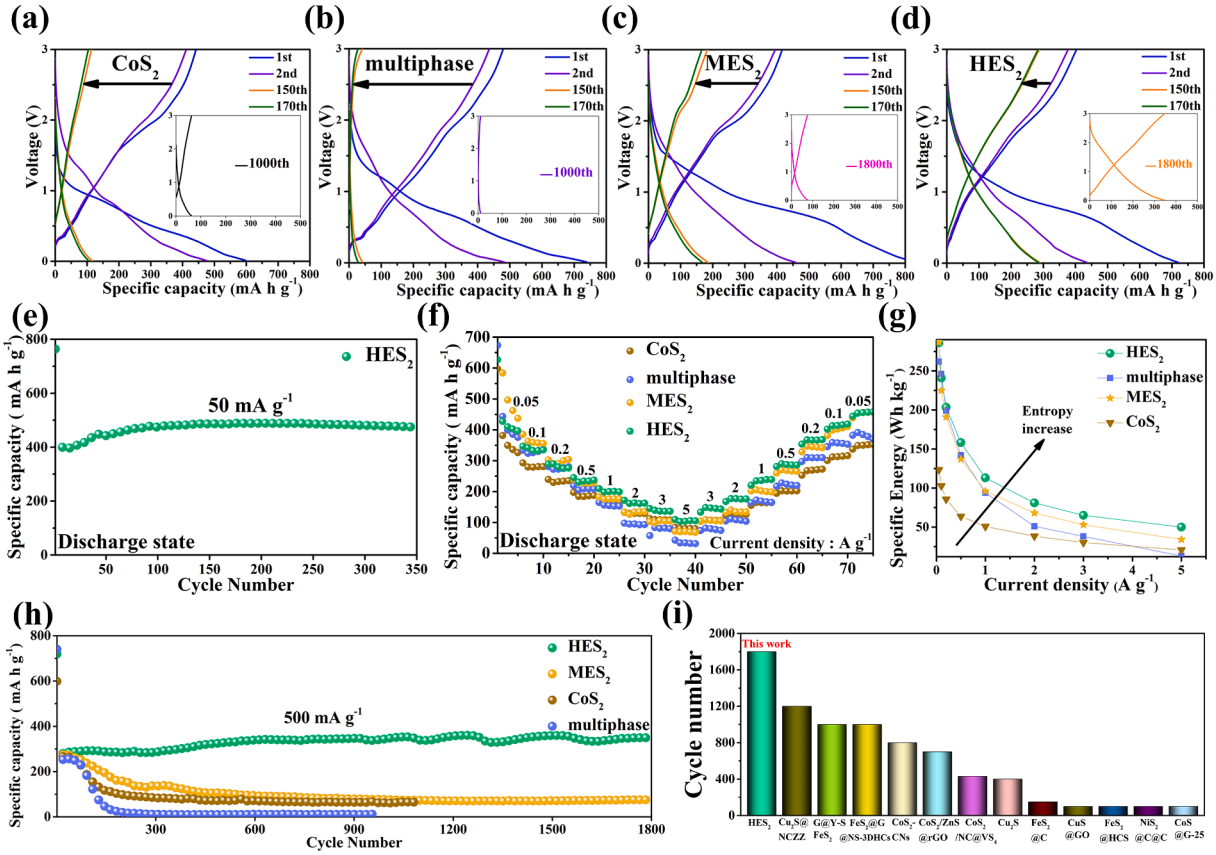

Fig. 3. Electrochemical performances characterization: Discharge-charge profiles of (a) CoS_2, (b) multiphase, (c) MES_2, and (d) HES_2 electrodes. (e) Cycling performances at 50 mA g^{-1}. (f) Rate capabilities and (g) Energy densities at different current densities of HES_2, MES_2, CoS_2 and multiphase. (h)Long-term cycling stability of HES_2, MES_2, CoS_2 and multiphase. (i) Comparison of cycling performance among the HES_2 and other reported PIBs anodes.

charge capacities of 185.9 and 183.4 mA h g^{-1} at the 150th cycle, which is almost twice of the capacities of the CoS_2 electrode. The battery finally provided discharge and charge capacities of 87.9 and 87.7 mA h g^{-1} after 700th cycle. For the HES_2 half-cell (ΔS_{conf} = 1.61 R), the battery provided discharge and charge capacities of 289.4 and 287.6 mA h g^{-1} at 150th cycle. The capacity of the HES_2 electrode exhibits a slightly increase after 100 cycles, which suggests the optimization and stabilization of the solid electrolyte interphase (SEI) layers [18]. Moreover, it maintained a highly reversible capacity of 348 mA h g^{-1} with a CE closed to 99.5 % (Fig. 3h). Thus, there is no obvious capacity fading after 1800 cycles, exhibiting the highest capacity and the best cycling stability among these materials. Only the HES_2 electrode has an obvious plateau (Fig. 3d) at the 1800th cycle, indicating its excellent reversibility. A higher mass loading (1 mg) of HES_2 electrode (Figure S16) also show similar cycling stability with 1200 cycles. The CV curves of the other sulfides were shown in Figure S17(b)~(d). The cycling performance of HES_2 was shown in the Figure S18. Kinetic analysis of HES_2, MES_2 and CoS_2 were shown in the Figure S19 ~ 21. In-situ EIS of HES_2 was shown in the Figure S22. To gain a deeper understanding of the superior electrochemical performance of the HES_2 electrode, we have provided EIS impedance spectra and SEM images after 150 cycles in Figures S23-25. Notably, the multiphase electrode exhibits the highest impedance among the four types of electrodes examined. In contrast, HES_2 has the smallest impedance, signifying efficient electron transport. Furthermore, surface cracks on the electrode can negatively affect electron transport and result in reduced K^+ kinetics [37]. Upon examination of the images, it is evident that the surface of the HES_2 electrode is virtually devoid of cracks, underlining its exceptional mechanical properties. Conversely, the multiphase electrode shows numerous surface cracks, which contribute to its inferior electrochemical performance. As shown in Fig. 3i, for transition metal sulfides of non-high entropy configurations, current densities higher than 500 mA g^{-1} and capacities higher than 200 mA g^{-1}, such as FeS_2@HCS [17], G@Y-S FeS_2 [38], CoS_2/ZnS@rGO [39], Cu_2S [40], FeS_2@C [41], and CoS@G-25 [42], using structural treatments to an extend life cycle to 1000 cycles. As for increasing the active sites, CoS_2-CNs [18] and CuS@GO [19] can only provide 800 cycles. FeS_2@G@NS-3DHCs [17] and NiS_2@C@C [43] with bifunctional carbons can also increase the lifespan to almost 1000 times. The nitrogen-doped Cu_2S@NC [44] and CoS_2/NC@VS_4 [45], which can increase the cycling life to 1200 times. In summary, the method of prolonging the lifespan until now is 1200 cycles at maximum. The HES_2 in this work can significantly increase to 1800 cycles, providing a new way to construct a long-term cycling life for metal sulfides.

In order to figure out the effect of the high entropy configuration on the rate performance and cycling performance, cyclic voltammetry (CV) curves of the initial five cycles of four sulfides were measured at a scan rate of 0.1 mV s^{-1} between 0.01 and 3.0 V (V vs. K^+/K), as shown in Fig. 4(a). During the first cathodic scan of HES_2, the peak at 0.97 V corresponded to the formation of the solid electrolyte interface (SEI) and a new phase K_xHES_2 generated by intercalation of K^+ into HES_2 [38,46]. Furthermore, a broad peak at 0.53 V indicated the formation of polysulfides (K_2S, K_2S_2, and K_2S_4). The high entropy alloy (HEA) generated during the discharge process wouldn't react with any carbon matrix and alkaline ions. There were two peaks at 1.31 V and 2.11 V in the anodic scan corresponding to a gradual depotassiation process [17]. The K_xHES_2 became the final product at the end of the charge. After that, a reduction peak appeared at 1.37 V during the subsequent discharge process. In the following scan, the curves of the second and the third scan were well-overlapped, implying a high reversibility and stable kinetics of potassium storage. The initial 5 cycles CV (Figure S17(b), (c)) of other electrodes (MES_2 and CoS_2) showed similar multi-step electrochemical reactions. However, their poor degree of overlapping implies their instability in the electrochemical tests. The in-situ XRD pattern of HES_2 with graphite was conducted to analyze the mechanism; however, the low-crystalline phase of K_xHES_2 cannot be detected through XRD analysis followed by the Scherrer's equation (Figure S26). The electrochemical mechanism of K^+ storage in the HES_2 electrode was studied by ex-situ XPS (as shown in Fig. 4b) for the initial discharging/charging process, including some key states of HRTEM images and SAED patterns. For the pristine sample, the cation valences were $Fe^{2+/3+}$, $Co^{2+/3+}$, $Ni^{2+/3+}$, Cu^{1+} and Cr^{3+}, respectively. After discharging to 0.01 V, the spectra of Fe 2p, Co 2p, Ni 2p, Cu 2p, and Cr 2p showed the reduction reaction to form M^0. $Fe^{2+/3+}$ to Fe^0 (710.3 and 721.2 eV) [27,47], $Co^{2+/3+}$ to Co^0 (778.4 and 794 eV) [48,49], $Ni^{2+/3+}$ to Ni^0 (852.1 and 870 eV) [47,50], Cu^{1+} to Cu^0 (932.4 and 952.1 eV) [27] and Cr^{3+} to Cr^0 (574.8 and 583.5 eV) [51]. For the anion S^{2-}, the spectrum showed that it changed from S^{2-} to K_2S (161.3 eV) [52]. When charged to 3 V, the binding energy could not be recovered to the initial state, indicating an irreversible structural transformation of HES_2. The ex-situ HRTEM images and SAED patterns of the HES_2 electrode at different (discharging) charging states during the first cycle was also evaluated, as presented in Fig. 4(b)~(i). For the HES_2 electrode discharged to 1.37 V (D1.37 V), the lattice fringes of 0.2618, 0.313, and 0.203 nm can be observed in the HRTEM images, indexed to (220), (111) and (111) crystal planes of K_2S, K_xHES_2 and HEA, respectively (Fig. 4b). At the same time, the ring patterns of SAED of K_2S, K_xHES_2, and HEA phases were detected (Fig. 4f), confirming a conversion reaction between HES_2 and intercalated K^+. With fully discharged to 0.01 V, the lattice fringes of 0.26 and 0.205 nm were well associated with (220) of K_2S and (111) of HEA, respectively (as presented in Fig. 4c). A lot of grain boundaries formed interconnected network, enabling fast potassium ion and electron transport to achieve high-rate capability. Besides, the corresponding SAED pattern confirmed that the coexistence of K_2S and HEA (Fig. 4g). When charged to 2.0 V (C2.0 V), some K_2S and HEA transformed into K_xHES_2 with corresponding lattice fringes (110), as shown (Fig. 4d). Eventually, when charged to 3.0 V (C3.0 V), K_xHES_2 (200) could be clearly observed in Fig. 4e. The ex-situ TEM and ex-situ XPS of HES_2, MES_2 and CoS_2 were supplied in the supporting information. (Figure S27 ~ S34) Based on these results, the reaction mechanism of HES_2 during potassiation and depotassiation is shown in Fig. 4j. In the initial potassiation process, HES_2 reacted with K^+ to form HEA + K_2S. In the depotassiation process, HEA was converted to K_xHES_2 as the final product.

The reaction formula was as follows:

$$HES_2 + xK^+ + xe^- \rightarrow HEA + K_2S \leftrightarrow K_xHES_2$$

We executed a chemical adsorption test to observe the adsorption effect. Taking HES_2, MES_2 and CoS_2 as the adsorbent to catch the potassium polysulfides. The experiments were performed by adding 5 mg of K_2S to 5 mL DMC solution. After full dissolution, 5 mg of the above adsorbents were added and aged for 3 h (Fig. 5a). Obviously, the solution's color became clearer since most of the polysulfides were adsorbed by HES_2. For the one with MES_2, its color was slightly changed to translucent. The color remained unchanged as it contains CoS_2. Therefore, the results indicated that HES_2 having a stronger interaction with potassium polysulfide. In order to visualize the shuttle effect of potassium polysulfide more clearly, we conducted a "transparent" cell [53]. The transparent cell was assembled with potassium metal as the counter electrode, the above three materials as the working electrodes, and 1 M KFSI-in-DMC as the electrolyte as shown in Fig. 5b [54]. There is no difference in the color of the electrolyte in the CoS_2 cell when discharged to 0.5 V. Upon further discharge to 0.01 V, the color of it gradually turned white, confirming the dissolution of potassium polysulfide and the shuttle effect. The white color slightly faded but still existed throughout the subsequent charging process. In contrast, the electrolyte color in the HES_2 cell remained pure after discharging to 0.01 V, implying that HEA could effectively adsorb polysulfides. In addition, the appearance of the yellow color on the separator surface after 20 cycles of CoS_2 and MES_2, while HES_2 was in the opposite condition from its strong inhibition of the shuttle effect (Figure S35). To compare the activity differences among the individual materials, linear cyclic voltammetry (LSV) was used, as shown in Fig. 5c. The HES_2 cell exhibited an early and

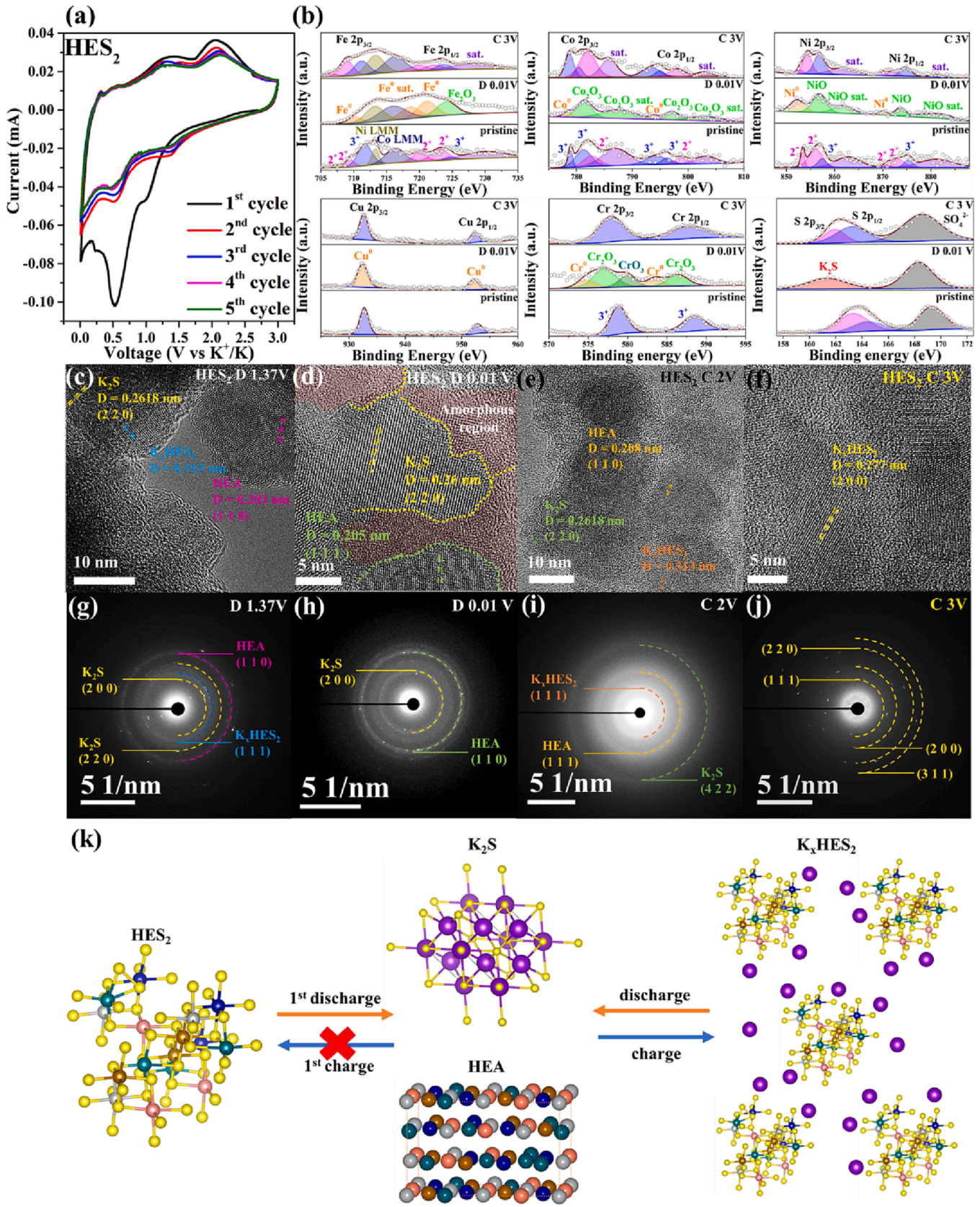

Fig. 4. Reaction mechanism of HES_2. (a) Cyclic voltammetry (CV) curves of initial five cycles of HES_2 (b) Ex situ XPS analysis of HES_2 electrodes before/after cycling. Comparison of the Fe 2p, Co 2p, Ni 2p, Cu 2p, and Cr 2p for the material in the pristine, fully discharged (D0.01 V) and fully charged (C3.0 V) states. Ex situ TEM and SAED patterns at discharging states of (c, g) 1.37 V and (d, h) 0.01 V and charging states of (e, i) 2.0 V and (f, j) 3.0 V. (k) Schematic illustration of the reaction mechanism of HES_2.

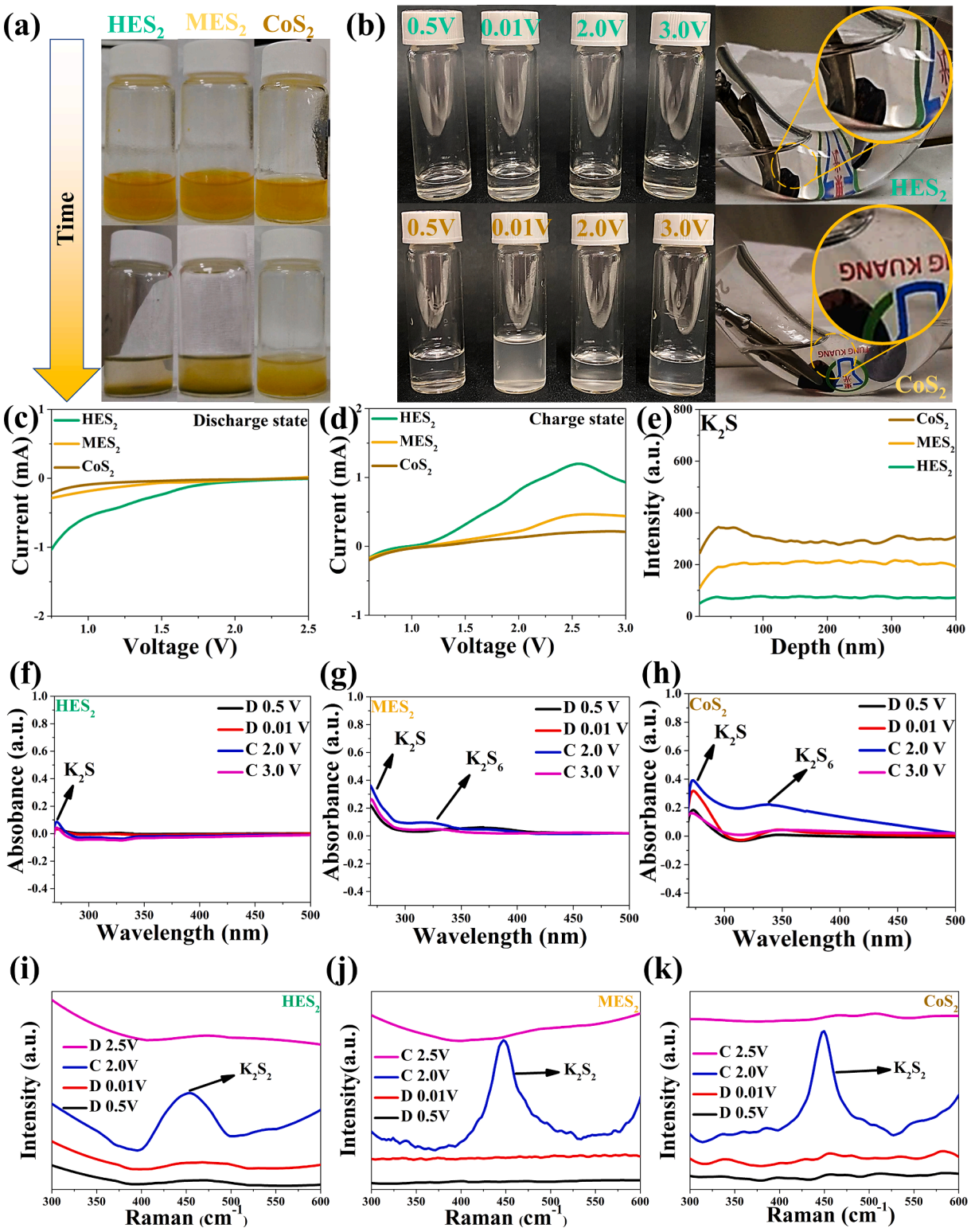

Fig. 5. (a) Polysulfides adsorption experiment of HES_2, MES_2 and CoS_2. (b) Transparent batteries of HES_2 and CoS_2 visualize the dissolution and shuttle effect behaviors of the polysulfides during the discharging/charging process. LSV of HES_2, MES_2 and CoS_2 in discharging state (c) and charging state (d). (e) TOF-SIMS depth profile of HES_2, MES_2 and CoS_2 for K_2S. UV–visible spectra at discharge voltages of 0.5 V (black), 0.01 V (red), and charge voltages of 2.0 V (blue), 3.0 V (pink) (f) for HES_2, (g) for MES_2 and (h) for CoS_2. Raman spectra at different voltages of 0.5 V (black), 0.01 V (red), and charge voltages of 2.0 V (blue), 2.5 V (pink) (i) for HES_2, (j) for MES_2 and (k) for CoS_2. (For interpretation of the references to color in this figure legend, the reader is referred to the web version of this article.)

broad peak during the cathodic scan, whereas the MES_2 and CoS_2 cells did not show any reduction peak. The HES_2 cell showed a much higher oxidation peak (2.5 V) and a weaker oxidation peak in the MES_2 cell, and there was no peak in the CoS_2 cell (Fig. 5d) [55]. In order to get into the adsorption ability of each material for potassium polysulfide, TOF-SIMS analysis was also conducted. TOF-SIMS analysis was a powerful technique for probing molecular information, demonstrating the adsorption status of each material for potassium polysulfide. Fig. 5 showed the

relative mass intensities at the electrode surfaces of HES_2, MES_2 and CoS_2 after 20 cycles. At the beginning of beam sputtering, the difference between them can be clearly observed. The intensity of K_2S at the electrode surface of CoS_2 is higher than that of MES_2, and even much higher than that of HES_2. Such results were consistent with the experiments in Fig. 5, b. To get into the polysulfide concentration changes of these three electrode materials during charging/discharging process, ex-situ UV–vis spectroscopy was used, as shown in Fig. 5, g, h. At charging (2.0 V, blue curve), the absorbance intensities of HES_2, MES_2 and CoS_2 electrodes were very high ($CoS_2 > MES_2 > HES_2$). It is worth mentioning that the absorbance intensity of the CoS_2 electrode was higher when discharged (0.01 V, red curve), but others were not. The increase in absorbance intensity indicates the increase in the concentration of K_2S in the electrolyte, confirming that HEA has excellent adsorption ability to potassium polysulfides [56,57]. To illustrate the adsorption of HES_2 to polysulfides during charging and discharging, the in-situ Raman was conducted (Figure S36). Throughout the potassiation process, the K_2S_2 peak emerges between 0.7 V and 0.01 V, indicating polysulfide formation. In the following depotassiation process, the K_2S_2 peak diminishes gradually and disappears at 2.4 V, indicating polysulfide adsorption. Moreover, ex-situ Raman analysis (as shown in Fig. 5i, j, k) also used. The band at 452 cm^{-1} could be identified as K_2S_2 [58,59]. The intensities of them were not obvious when discharged to 0.5 V and 0.01 V (black curve, red curve). When charged to 2.0 V (blue curve), both MES_2 and CoS_2 have a strong peak at 452 cm^{-1}, while HES_2 has a weaker peak intensity. When charged to 2.5 V (pink curve), the peak at 452 cm^{-1} disappeared, indicating the reaction was reversible. The above result is also the same as Fig. 5(a), (b), (e), (f), (g) and (h). In conclusion, HES_2 has a more excellent adsorption ability than MES_2 and CoS_2.

We conducted DFT calculations to further investigate the catalytic effects of different alloys (metals) produced discharged to 0.01 V. We present the density of states (DOS) of three metals: HEA, MEA (FeCoNiCu) and pure Co metal. Pure Co metal demonstrated the highest d-band center (-2.44 eV) due to its free electrons and similar atomic properties, which allow for metal bonding. While most of chemical bonds of HEA and MEA have mostly metal bonds, some electrons are localized between atoms, forming covalent bonds. Thus, HEA and MEA possess lower d-band centers (HEA:-2.69 eV, MEA:-2.77 eV). Moreover, HEA has stronger interatomic forces compared to MEA, showing that high entropy is beneficial to stabilize the crystal structure. Fig. 6b summarized the comparison of adsorption energy E_{ad} for K_2S. Wider surface d-bands can push more states to higher energies, leading to higher energy adsorption-antibonding states and stronger adsorption bonding. Our calculations show that HEA exhibits the most remarkable E_{ad} (-2.97 eV), corresponding to the calculated DOS in Fig. 5a, followed by MEA (-2.21 eV), and pure Co metal (-2.14 eV) was the worst. Fig. 6c illustrates the electron aggregation and depletion regions in yellow and blue, respectively. The two-dimensional electron density difference diagram enables the visualization of the ability of elements to gain and lose electrons. As depicted in Fig. 6d, introducing elements with lower electronegativity (such as Fe (1.83) and Cr (1.66)) reduce the valence state of S, allowing it to carry more negative charges. Consequently, this enhances the electrostatic interaction with K^+ and improve the adsorption of K_2S. HEA contains Fe and Cr proving the best adsorption energy, while lacking Cr makes MEA has weaker adsorption energy. Pure Co metal has neither element, exhibiting the weakest adsorption energy. Notably, the adsorption energy of MEA still surpasses that of pure Co, indicating that the introduction of Fe benefits the adsorption of polysulfides. Furthermore, other metal elements (Ni, Cu, and Co) are beneficial to multi-electron reactions from their ability to charge regulation.

Using the exceptional cycling performance of HES_2 in half cells, as well as its high entropy configuration which improves the shuttle effect commonly found in chalcogenide electrodes, we have combined HES_2 with materials typically used in the positive electrode of potassium ion batteries to create potassium ion full cells. However, due to the high oxidation potential of polysulfide K_2S, certain cathode materials such as PTCDA [60] and $KVPO_4F$ cannot meet the required high working voltage of over 3.5 V, so the Prussian analogues with high working voltage were utilized [61–63]. Fig. 7a shows a schematic diagram illustrating the reaction of the full cell in charging state, referred to as HES_2//PB, with HES_2 serving as the negative electrode, PB as the positive electrode, and 1 M KFSI DMC as the electrolyte. The PB positive electrode was synthesized via a co-precipitation method [64], resulting in a stable structure capable of receiving potassium ions transported from the negative electrode. The XRD pattern of PB was shown in the Figure S37. According to the charging/discharging curve presented in Figure S38, the PB half-cell delivered a capacity of 63 mA h g^{-1} when the working window ranged from 2 to 4 V. We also tested the CV curves of PB at different scan rates (Figure S39). Before assembling the full cell, it was necessary to balance the charge by adjusting the mass ratio of the negative electrode to the positive electrode (N:P = 1:6). HES_2//PB was cycled at 60 mA g^{-1} in the working window ranging from 1 V to 3.8 V, ultimately obtaining a discharge voltage of 3.25 V. In Fig. 7(b), the green

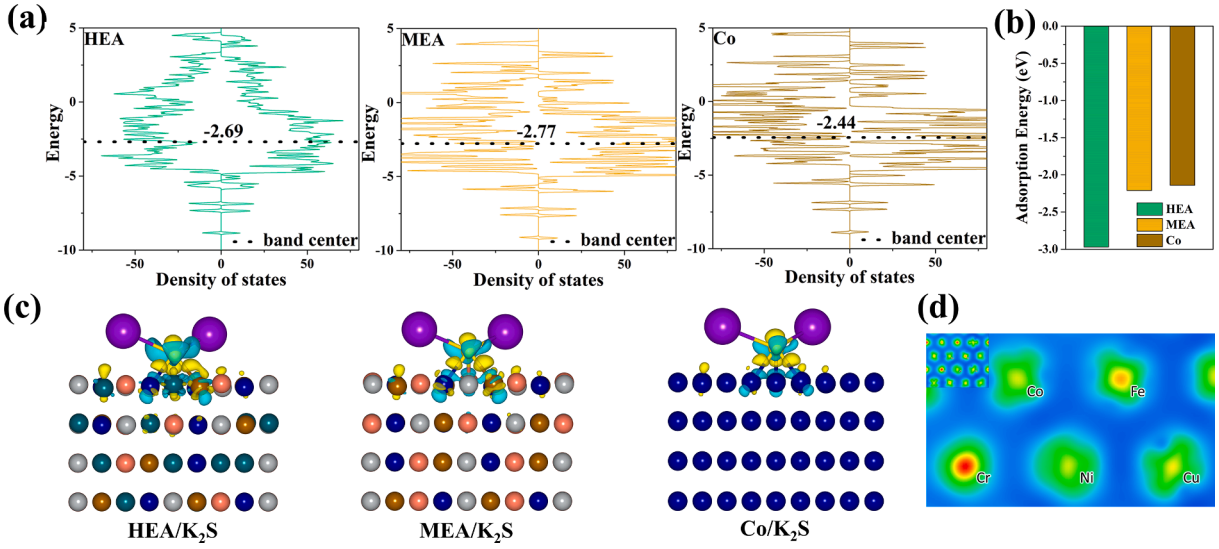

Fig. 6. (a)The DOS of HEA, MEA and Co metal. (b) Comparison of adsorption ability of HEA, MEA and Co metal for K_2S. (c) Differential charge density diagrams of K_2S on the (1 1 1) surface of HEA, MEA and Co metal. (d) 2D electron density differences of HEA.

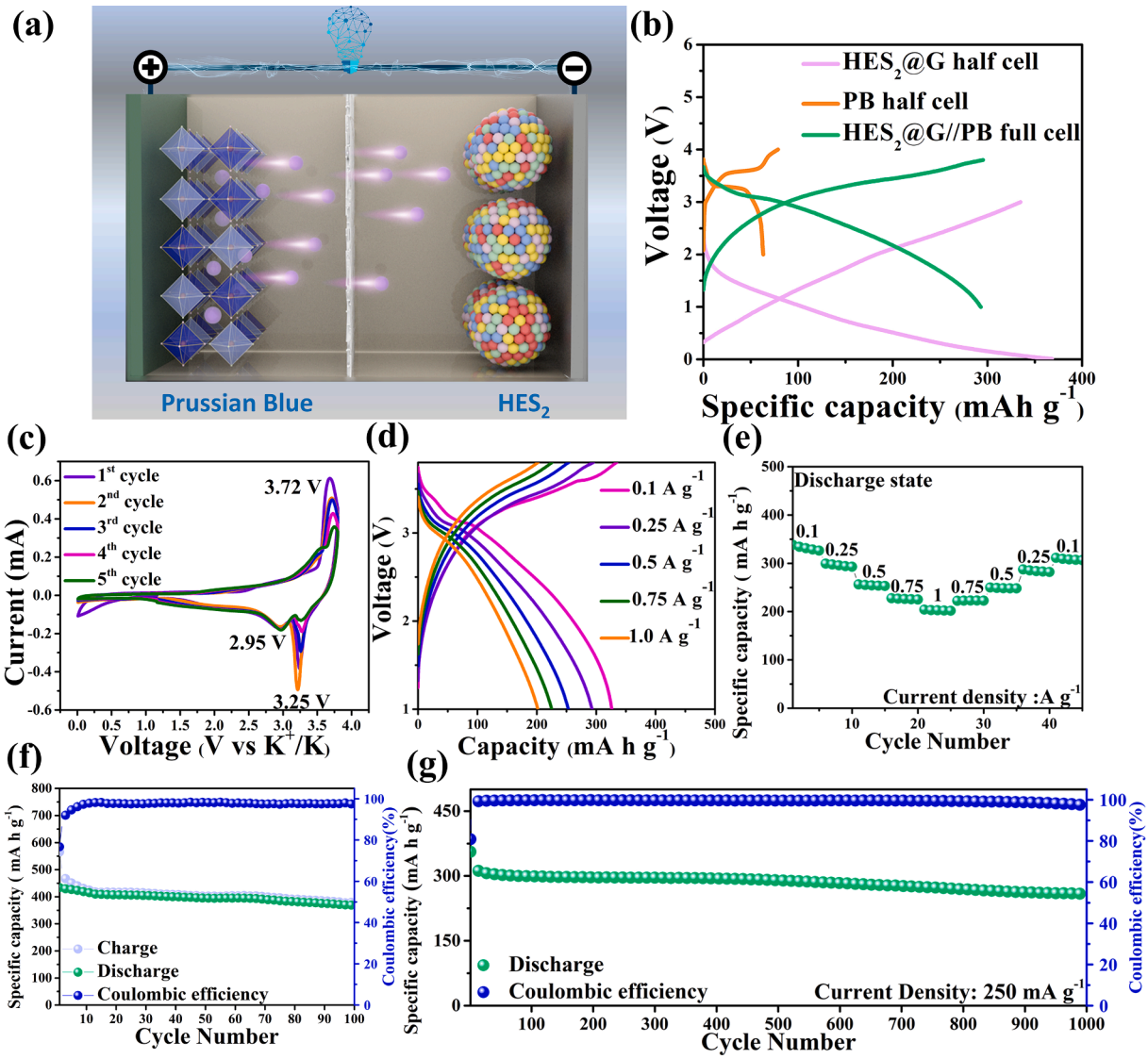

Fig. 7. (a) Schematic diagram of a HES_2@G//PB full cell. (b) Discharge/charge curves of PB and HES_2@G half cells and a HES_2@G//PB full cell. (c) The CV profiles of a HES_2@G//PB full cell at a scan rate of 1.0 mV s^{-1}. (d, e) Rate capability when the current densities are ranging from 0.1 to 1.0 mA g^{-1}. (f) Cycling performance of a HES_2@G//PB full cell at 50 mA g^{-1}. (g) Long-term cycling performance of a HES_2@G//PB full cell at 250 mA g^{-1}.

curve exhibits two significant plateaus, namely the 3.25 V discharging plateau and the 3.72 V charging plateau. Meanwhile, Fig. 7(c) illustrates the cyclic voltammogram (CV) curves of HES_2//PB at a scan rate of 1.0 mV s^{-1}, where the high reversibility and cycling stability of HES_2//PB are evident from the well-overlapped curves. Furthermore, the rate performance of HES_2//PB was tested at various current densities of 100, 250, 500, 750, and 1000 mA g^{-1}, as shown in Fig. 7(e), with corresponding discharge capacities of 326, 292, 253, 225, and 201 mA h g^{-1} based on the anode's mass. It is worth noting that there was a loss of discharge capacity of approximately 10–15 % in each interval. Even when the current density returned to 100 mA g^{-1}, HES_2//PB still exhibited a discharge capacity of 306 mA g^{-1}. At high current densities, there was a slight overpotential, resulting in a plateau shift, but HES_2//PB still maintained an excellent energy density. Additionally, the plotted GCD curves in Fig. 7(d) correspond to the tested rate performance at various current densities. The full cell's cycling capability was tested at a low current density of 50 mA g^{-1}, as shown in Fig. 7(f), while Fig. 7(g) demonstrated the long-term cycling stability of the full cell, which maintained an excellent capacity retention of 83.1 % after 1000 cycles at a current density of 250 mA g^{-1} with an average CE of about 99.4 %.

Furthermore, we constructed potassium-ion hybrid capacitors (PIHCs) using capacitive electrodes as cathodes and battery-type electrodes as anodes, taking advantage of the high reaction kinetics and potassium storage capacity of HES_2 [65,66] Specifically, we used HES_2 with graphite as a high-power anode, and a commercially available activated carbon (AC) as a high-energy cathode [67]. Prior to assembling the PIHCs, we pre-activated the anode of HES_2 with graphite for 20 cycles to activate the electrode and minimize the irreversible capacity loss of the initial cycle. To prevent electrolyte decomposition, the working voltage was limited to 0.5–3.8 V. The mass ratio of HES_2 and AC was the best mass ratio of 1:1 to maximize output power. We further investigated the electrochemical performance of HES_2//AC, and the typical CV curves of the successfully assembled PIHCs are presented in Fig. 8(a). The charge–discharge curves of the HES_2//potassium half-cell, AC//potassium half-cell, and HES_2//AC full-cell are shown in Fig. 8(b), exhibiting typical capacitor behavior with approximately linear charge/discharge curves. The AC//potassium half-cell was also tested with CV at different scan rates (Fig. 8c). The GCD curves of HES_2//AC at different current densities was measured (Fig. 8d), and a small charge–discharge slope was observed due to the mechanism of Faradaic and non-Faradaic reactions in the anode and cathode. In addition, we tested the energy density of HES_2//AC at different current densities based on the total

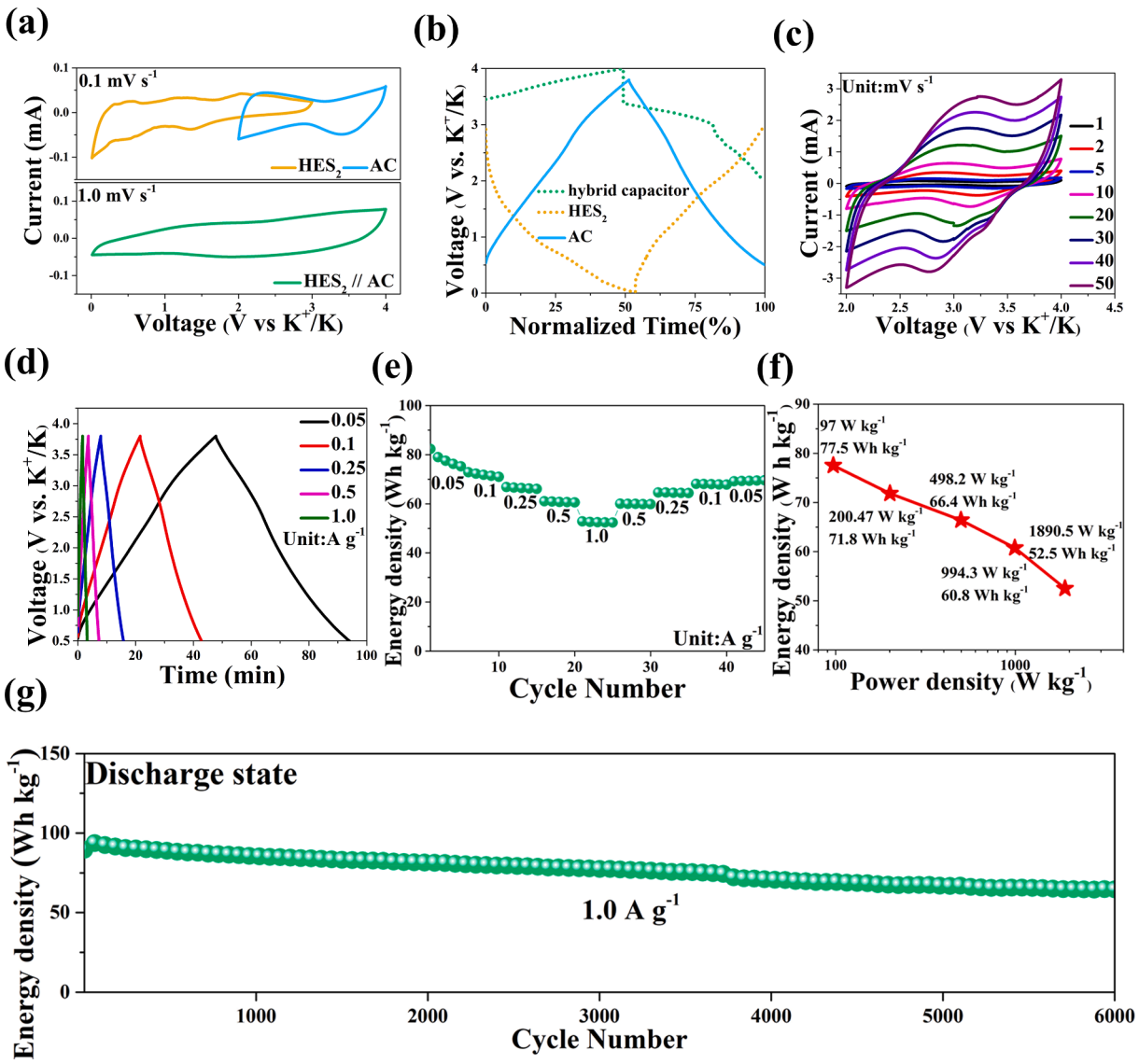

Fig. 8. (a) CV curves of the AC half cell, HES_2@G half cell and the HES_2@G//AC PIHCs. (b) Normalized GCD curves of the AC half cell, HES_2@G half cell and the HES_2@G//AC PIHCs. (c) AC half cell CV profiles at different scan rate ranging from 1.0 mV s^{-1} to 50 mV s^{-1}. (d) Normalized GCD curves plotted corresponded to rate capability and (e) Rate capability performance. (f) Ragone plot of the HES_2@G//AC PIHCs. (g) Long-term cycling performance of the HES_2@G//AC PIHCs at 1.0 A g^{-1}.

weight of HES_2 with graphite and activated carbon (Fig. 8e). Even at high current densities of 0.05, 0.1, 0.25, 0.5, and 1.0 A g^{-1}, HES_2//AC still produced energy densities of 75, 71, 66, 60, and 52 Wh kg^{-1}. The energy power density of HES_2//AC PIHCs is presented in the Ragone diagram of Fig. 8f, demonstrating a high energy density of 77.5 Wh kg^{-1} and a power density of 1890.5 W kg^{-1}. Notably, HES_2//AC exhibited ultra-long cycling performance, maintaining 71.5 % of its initial capacity after 6000 cycles at a high current density of 1000 mA g^{-1} (Fig. 8g).

3. Conclusion

We propose a high entropy template composed of five cations (Fe, Co, Ni, Cu, Cr) uniformly distributed, which is then solvothermally sulfurized into sphere composed of aggregated HES_2 clusters to serve as anodes materials for potassium ion storage devices. The HES_2 nanoscale materials are beneficial in shortening the diffusion path of potassium ions. During the charging/discharging process, the materials disperse into uniformly distributed heterogeneous grains, increasing the reactive area and improving chemical kinetics to achieve high performance. Our experiments, coupled with DFT simulations, the adsorption ability increases with the configurational entropy from gradually metal-introducing process. Due to the effective inhibition of the shuttle effect, the HES_2 anodes in both full cells and PIHCs demonstrate high feasibility and cyclability, thus providing a reliable idea for designing chalcogenide electrode systems. We believe this work can promote the development of chalcogenides in the field of materials science and electrochemical reactions for next-generation storage systems and have a pioneering impact.

4. Experimental section

4.1. Materials

$Co(NO_3)_2{\cdot}6H_2O$ (Alfa Aesar, 99 %), $Cr(NO_3)_2{\cdot}9H_2O$ (Alfa Aesar, 98.5 %), $Fe(NO_3)_3{\cdot}9H_2O$ (J.T. Baker, 99 %), $Ni(NO_3)_3{\cdot}6H_2O$ (Alfa Aesar, 98.5 %), $Cu(NO_3)_2{\cdot}2.5H_2O$ (Sigma-Aldrich, 98.5 %), glycerol (Honeywell, 99 %), and thiourea (Sigma-Aldrich, 99 %) were used as the

precursors. Isopropanol (J.T. Baker, 99.5 %) and ethanol (99.9 %) were used as the solvents. Sodium carboxymethyl cellulose (NaCMC, average $M_w \sim 700{,}000$), dimethyl carbonate (DMC, anhydrous 99 %), 1-Methyl-2-pyrrolidinone(NMP, anhydrous, 99.5 %) and potassium metal (chunks in mineral oil, 98 %) were purchased from Sigma-Aldrich. Potassium bis (fluorosulfonyl)imide (KFSI, 97 %) was purchased from Combi-Blocks. Super-P, and coin-type cell CR2032 were purchased from shining energy. Glass fiber was purchased from Advantec. Copper foil were purchased from Chang-Chun group. All the chemicals were used without purification.

4.2. Material characterization

All materials were characterized by using scanning electron microscopy (SEM, HITACHI-SU8010), X-ray photoelectron spectroscopy (XPS, ULVAC-PHI, PHI Quantera II) transmission electron microscopy (TEM, JEOL, JEM-ARM200FTH) and X-ray diffraction (XRD, Bruker D8 ADVANCE). To obtain HRSEM images of materials, a HITACHI-SU8010 field-emission SEM with 10 kV accelerating voltage and 8 mm working distance were utilized. The TEM samples were prepared by drop-casting the composite from ethanol dispersions onto 200-mesh lacey carbon-coated copper grids and gold grids (Electron Microscope Sciences) following dried at 45℃ with argon atmosphere for 14hrs. Meanwhile, XRD patterns were obtained by a Bruker D8 ADVANCE diffractometer equipped with Cu Kα radiation.

4.3. Synthesis of HES_2

High entropy glycerate templates were first synthesized using a facile solvothermal process as reported previously. In brief, $Fe(NO_3)_3{\cdot}9H_2O$ (0.2 g), $Ni(NO_3)_3{\cdot}6H_2O$(0.1454 g), $Co(NO_3)_2{\cdot}6H_2O$ (0.1455 g), $Cr(NO_3)_2{\cdot}9H_2O$ (0.2 g), and $Cu(NO_3)_2{\cdot}2.5H_2O$ (0.11628 g) were dissolved in 34 mL isopropanol, followed by the addition 6 mL of glycerol. Homogeneously mixed solution was transferred to a 100 mL Teflon-lined stainless-steel autoclave for solvothermal reaction at 150 °C for 10 hrs. The resulting powders were collected and used as the templates for the metal sulfides synthesis. To prepare the HES_2 nanoclusters, 100 mg of the as-synthesized metal glycerate was dispersed in 50 mL of absolute ethanol, followed by the addition of 380 mg of thiourea. The mixture was then cooling stirred for 30 min before transferring to a 100 mL Teflon-lined stainless-steel autoclave. The temperature and time for the solvothermal synthesis were 160 °C and 8 h, respectively. The product was centrifuged and washed three times with absolute ethanol and then dried at 60 °C for 24 h in a vacuum oven. Controlling samples of single metal sulfides (CoS_x), quinary metal sulfides ($FeNiCoCuS_2$) were prepared using the same method using the corresponding as-synthesized metal glycerate templates.

4.4. Synthesis of HES_2 with graphite composite

60 mg of as-prepared HES_2 and 30 mg of graphite were put into a stainless-steel milling jar (12 mL) with stainless steel balls (10 mm in diameter), the weight ratio of ball to powder was about 178:1. and sealed the jar in an Ar-filled glove box. By high-energy mechanical ball-milling method at 200 rpm for 24 h, HES_2 with graphite composite was obtained.

4.5. Synthesis of Prussian blue (PB)

0.005 mol of $FeCl_2{\cdot}4H_2O$ (Sigma Aldrich, 98 %) dissolved in 0.05 L of DI water as solution A. 0.005 mol of $K_4Fe(CN)_6{\cdot}3H_2O$ (Sigma Aldrich, 99.5 %), 0.01 mol of potassium citrate, 0.2 mol of KCl (PubChem, 99 %) and 0.003 mol of ascorbic acid (Sigma Aldrich, $>$ 99 %) were dissolved in 0.1 L of DI water as solution B. Solution A was slowly added into solution B. The dark blue solid product was centrifuged and washed three times with DI water, and finally dried at 100 °C in a vacuum furnace for 16 hrs.

4.6. Electrochemical measurement

The anode electrode was prepared by mixing active material (HES_2/graphite with the ratio of 2:1), super P, NaCMC, PAA in the ratio of 7:2:0.5:0.5 in distilled water and absolute ethanol to form a homogeneous slurry. The slurry was coated on the copper foil by doctor blade and dried at 80℃ under argon atmosphere. The mass loading of anode was roughly 0.6 $\sim$ 1.0 mg cm^{-2}. The mass loading of electrode was measured by microbalance with 0.1 μg resolution (Sartorius SE2). The cyclic voltammetry (CV) was collected by multi-channel electrochemical analyzer (Bio-Logic-science Instruments, VMP3). Generally, graphite is considered to has some specific capacity contribution, so the specific capacity calculation of HES_2 electrode is based on total mass of graphite and HES_2. The coin-type half-cell (CR2032) was assembled in an argon filled glovebox (H_2O and $O_2 \leqq 0.1$ ppm) using homemade K metal foil as a counter electrode. The electrolyte composed of 1 M KFSI in DMC was added to infiltrate the anode electrode and glass fiber separator was added, followed by the K foil. After crimping, the battery was taken out from glovebox and tested the electrochemical performance by the Maccor Series 4000 battery test system with the voltage ranging from 0.01 V to 3.0 V.

4.7. Computational section

All the first-principle density functional theory (DFT) calculations were performed by Vienna Ab-initio Simulation Package (VASP). The Perdew-Burke-Ernzerh (PBE) in the generalized gradient approximation (GGA) was applied to describe the exchange–correlation function. Based on the plane wave method, the projector augmented-wave (PAW) method with an energy cutoff of 400 eV was implemented for the electron–ion interactions. All structures were fully relaxed until the electronic energy and force acting on atom were smaller than 10^{-4} eV and 0.02 eV·$Å^{-1}$, respectively. The Brillouin-zone sampling were conducted using Monkhorst-Pack (MP) grids of special points with the separation of 0.04 $Å^{-1}$. A Gaussian smearing of 0.05 eV was applied to speed up self-consistent field iteration. Based on the bulk Co cell, the corresponding partial Co atoms were randomly replaced by Fe, Co, Ni, Cu, and Cr to build the HEA models. The 4-layer 4 $\times$ 4 supercell of Co (1 1 1), CoFeNiCu(1 1 1), and CoFeNiCoCr(1 1 1) slab were used to build the K_2S adsorption calculation models. The optimized structures and charge density difference distribution were illustrated with VESTA software.

Declaration of Competing Interest

The authors declare that they have no known competing financial interests or personal relationships that could have appeared to influence the work reported in this paper.

Data availability

No data was used for the research described in the article.

Acknowledgments

This work was supported by the financial support from the 2030 Cross-Generation Young Scholars Program by National Science and Technology Council, Taiwan (NSTC 112-2628-E-007-010). H.-Y. Tuan also acknowledges the financial support of National Tsing Hua University, Taiwan, through Grant No. 112B0011J2. The authors thank Ms. Y. M. Chang (Instrumentation center at NTHU) for spherical-aberration corrected field emission TEM analysis.

Appendix A. Supplementary data

Supplementary data to this article can be found online at https://doi.org/10.1016/j.cej.2023.143942.

References

[1] C. Lv, X. Zhou, L. Zhong, C. Yan, M. Srinivasan, Z.W. Seh, C. Liu, H. Pan, S. Li, Y. Wen, Q. Yan, Machine learning: an advanced platform for materials development and state prediction in lithium-ion batteries, Adv. Mater. 34 (25) (2022) 2101474, https://doi.org/10.1002/adma.202101474.

[2] D. Wang, S. Jiang, C. Duan, J. Mao, Y. Dong, K. Dong, Z. Wang, S. Luo, Y. Liu, X. Qi, Spinel-structured high entropy oxide $(FeCoNiCrMn)_3O_4$ as anode towards superior lithium storage performance, J. Alloys Compd. 844 (2020), 156158, https://doi.org/10.1016/j.jallcom.2020.156158.

[3] C. Duan, K. Tian, X. Li, D. Wang, H. Sun, R. Zheng, Z. Wang, Y. Liu, New spinel high-entropy oxides $(FeCoNiCrMnXLi)_3O_4$ (X= Cu, Mg, Zn) as the anode material for lithium-ion batteries, Ceram. Int. 47 (22) (2021) 32025–32032, https://doi.org/10.1016/j.ceramint.2021.08.091.

[4] K. Song, C. Liu, L. Mi, S. Chou, W. Chen, C. Shen, Recent progress on the alloy-based anode for sodium-ion batteries and potassium-ion batteries, Small 17 (9) (2021) 1903194, https://doi.org/10.1002/smll.201903194.

[5] W. Zhang, J. Mao, S. Li, Z. Chen, Z. Guo, Phosphorus-based alloy materials for advanced potassium-ion battery anode, J. Am. Chem. Soc. 139 (9) (2017) 3316–3319, https://doi.org/10.1021/jacs.6b12185.

[6] C. Zhang, H. Zhao, Y. Lei, Recent research progress of anode materials for potassium-ion batteries, EEM 3 (2) (2020) 105–120, https://doi.org/10.1002/eem2.12059.

[7] X. Yu, X. Ren, Z. Yuan, X. Hou, T. Yang, M. Wang, Ni_3S_2–Ni hybrid nanospheres with intra-core void structure encapsulated in N-doped carbon shells for efficient and stable K-ion storage, Adv. Sci. 10 (5) (2023) 2205556, https://doi.org/10.1002/advs.202205556.

[8] M. Qian, W. Zhang, G. Luo, C. Wu, W. Qin, Air-stabilized pore structure engineering of antimony-based anode by electrospinning for potassium ion batteries, J. Colloid Interface Sci. 633 (2023) 352–361, https://doi.org/10.1016/j.jcis.2022.11.121.

[9] J. Yang, Z. Ju, Y. Jiang, Z. Xing, B. Xi, J. Feng, S. Xiong, Enhanced capacity and rate capability of nitrogen/oxygen dual-doped hard carbon in capacitive potassium-ion storage, Adv. Mater. 30 (4) (2018) 1700104, https://doi.org/10.1002/adma.201700104.

[10] L. Xu, Z. Gong, C. Zhang, N. Li, Z. Tang, J. Du, A mushroom derived biomass carbon as high-stability anode for potassium ion battery, J. Alloys Compd. 934 (2023), 167820, https://doi.org/10.1016/j.jallcom.2022.167820.

[11] C.-Y. Tsai, C.-H. Chang, T.-L. Kao, K.-T. Chen, H.-Y. Tuan, Shape matters: $SnP_{0.94}$ teardrop nanorods with boosted performance for potassium ion storage, Chem. Eng. J. 417 (2021), 128552, https://doi.org/10.1016/j.cej.2021.128552.

[12] S.-F. Ho, H.-Y. Tuan, Cu_3PS_4: a sulfur-rich metal phosphosulfide with superior ionic diffusion channel for high-performance potassium ion batteries/hybrid capacitors, Chem. Eng. J. 452 (2023), 139199, https://doi.org/10.1016/j.cej.2022.139199.

[13] J. Wu, S. Liu, Y. Rehman, T. Huang, J. Zhao, Q. Gu, J. Mao, Z. Guo, Phase engineering of nickel sulfides to boost sodium-and potassium-ion storage performance, Adv. Funct. Mater. 31 (27) (2021) 2010832, https://doi.org/10.1002/adfm.202010832.

[14] C. Lu, Z. Sun, L. Yu, X. Lian, Y. Yi, J. Li, Z. Liu, S. Dou, J. Sun, Enhanced kinetics harvested in heteroatom dual-doped graphitic hollow architectures toward high rate printable potassium-ion batteries, Adv. Energy Mater. 10 (28) (2020) 2001161, https://doi.org/10.1002/aenm.202001161.

[15] L. Yang, W. Hong, Y. Tian, G. Zou, H. Hou, W. Sun, X. Ji, Heteroatom-doped carbon inlaid with Sb_2X_3 (X= S, Se) nanodots for high-performance potassium-ion batteries, Chem. Eng. J. 385 (2020), 123838, https://doi.org/10.1016/j.cej.2019.123838.

[16] L. Zhang, M. Zhang, H. Guo, Z. Tian, L. Ge, G. He, J. Huang, J. Wang, T. Liu, I. P. Parkin, F. Lai, A universal polyiodide regulation using quaternization engineering toward high value-added and ultra-stable zinc-iodine batteries, Adv. Sci. 9 (13) (2022) 2105598, https://doi.org/10.1002/advs.202105598.

[17] B. Chen, J. Ding, X. Bai, H. Zhang, M. Liang, S. Zhu, C. Shi, L. Ma, E. Liu, N. Zhao, F. He, W. Zhou, C. He, Engineering pocket-like graphene-shell encapsulated FeS_2: inhibiting polysulfides shuttle effect in potassium-ion batteries, Adv. Funct. Mater. 32 (14) (2022) 2109899, https://doi.org/10.1002/adfm.202109899.

[18] H. Zhang, Y. Cheng, J. Sun, W. Ye, C. Ke, M. Cai, H. Gao, P. Wei, Q. Zhang, M. S. Wang, Anti-aggregation of nanosized CoS_2 for stable K-ion storage: insights into aggregation-induced electrode failures, Adv. Energy Mater. 12 (29) (2022) 2201259, https://doi.org/10.1002/aenm.202201259.

[19] X. Jia, E. Zhang, X. Yu, B. Lu, Facile synthesis of copper sulfide nanosheet@graphene oxide for the anode of potassium-ion batteries, Energy Technol. 8 (1) (2020) 1900987, https://doi.org/10.1002/ente.201900987.

[20] L. Wu, X. Shen, Z. Ji, J. Yuan, S. Yang, G. Zhu, L. Chen, L. Kong, H. Zhou, Facile synthesis of medium-entropy metal sulfides as high-efficiency electrocatalysts toward oxygen evolution reaction, Adv. Funct. Mater. 33 (3) (2023) 2208170, https://doi.org/10.1002/adfm.202208170.

[21] L. Lin, K. Wang, A. Sarkar, C. Njel, G. Karkera, Q. Wang, R. Azmi, M. Fichtner, H. Hahn, S. Schweidler, B. Breitung, High-entropy sulfides as electrode materials for li-ion batteries, Adv. Energy Mater. 12 (8) (2022) 2103090, https://doi.org/10.1002/aenm.202103090.

[22] M.A. Buckingham, B. Ward-O'Brien, W. Xiao, Y. Li, J. Qu, D.J. Lewis, High entropy metal chalcogenides: synthesis, properties, applications and future directions, ChemComm 58 (58) (2022) 8025–8037, https://doi.org/10.1039/D2CC01796B.

[23] M. Cui, C. Yang, B. Li, Q. Dong, M. Wu, S. Hwang, H. Xie, X. Wang, G. Wang, L. Hu, High-entropy metal sulfide nanoparticles promise high-performance oxygen evolution reaction, Adv. Energy Mater. 11 (3) (2021) 2002887, https://doi.org/10.1002/aenm.202002887.

[24] F.-W. Yuan, H.-J. Yang, H.-Y. Tuan, Seeded silicon nanowire growth catalyzed by commercially available bulk metals: broad selection of metal catalysts, superior field emission performance, and versatile nanowire/metal architectures, J. Mater. Chem. 21 (36) (2011) 13793–13800, https://doi.org/10.1039/C1JM11956G.

[25] K. Chu, J. Qin, H. Zhu, M. De Ras, C. Wang, L. Xiong, L. Zhang, N. Zhang, J. A. Martens, J. Hofkens, F. Lai, T. Liu, High-entropy perovskite oxides: a versatile class of materials for nitrogen reduction reactions, SCMs 65 (10) (2022) 2711–2720, https://doi.org/10.1007/s40843-022-2021-y.

[26] B. Jiang, Y. Yu, J. Cui, X. Liu, L. Xie, J. Liao, Q. Zhang, Y. Huang, S. Ning, B. Jia, B. Zhu, S. Bai, L. Chen, S.J. Pennycook, J. He, High-entropy-stabilized chalcogenides with high thermoelectric performance, Science 371 (6531) (2021) 830–834, https://doi.org/10.1126/science.abe1292.

[27] J. Zhao, Y. Zhang, X. Chen, G. Sun, X. Yang, Y. Zeng, R. Tian, F. Du, Entropy-change driven highly reversible sodium storage for conversion-type sulfide, Adv. Funct. Mater. 32 (45) (2022) 2206531, https://doi.org/10.1002/adfm.202206531.

[28] Y. Ma, Y. Ma, S.L. Dreyer, Q. Wang, K. Wang, D. Goonetilleke, A. Omar, D. Mikhailova, H. Hahn, B. Breitung, T. Brezesinski, High-entropy metal-organic frameworks for highly reversible sodium storage, Adv. Mater. 33 (34) (2021) 2101342, https://doi.org/10.1002/adma.202101342.

[29] J. Jiang, S. Lu, H. Gao, X. Zhang, H.-Q. Yu, Ternary $FeNiS_2$ ultrathin nanosheets as an electrocatalyst for both oxygen evolution and reduction reactions, Nano Energy 27 (2016) 526–534, https://doi.org/10.1016/j.nanoen.2016.07.032.

[30] A. Papaderakis, N. Pliatsikas, C. Prochaska, K.M. Papazisi, S.P. Balomenou, D. Tsiplakides, P. Patsalas, S. Sotiropoulos, Ternary Pt-Ru-Ni catalytic layers for methanol electrooxidation prepared by electrodeposition and galvanic replacement, Front. Chem. 2 (2014) 29, https://doi.org/10.3389/fchem.2014.00029.

[31] Z.-Y. Tian, P.M. Kouotou, A. El Kasmi, P.H.T. Ngamou, K. Kohse-Höinghaus, H. Vieker, A. Beyer, A. Gölzhäuser, Low-temperature deep oxidation of olefins and DME over cobalt ferrite, Proc. Combust. Inst 35 (2) (2015) 2207–2214, https://doi.org/10.1016/j.proci.2014.06.111.

[32] W. Lai, Z. Chen, J. Zhu, L. Yang, J. Zheng, X. Yi, W. Fang, A NiMoS flower-like structure with self-assembled nanosheets as high-performance hydrodesulfurization catalysts, Nanoscale 8 (6) (2016) 3823–3833, https://doi.org/10.1039/C5NR08841K.

[33] G. Ai, Q. Hu, L. Zhang, K. Dai, J. Wang, Z. Xu, Y. Huang, B. Zhang, D. Li, T. Zhang, G. Liu, W. Mao, Investigation of the nanocrystal CoS_2 embedded in 3D honeycomb-like graphitic carbon with a synergistic effect for high-performance lithium sulfur batteries, ACS Appl. Mater. Interfaces 11 (37) (2019) 33987–33999, https://doi.org/10.1021/acsami.9b11561.

[34] H. Van der Heide, R. Hemmel, C. Van Bruggen, C. Haas, X-ray photoelectron spectra of 3d transition metal pyrites, J. Solid State Chem. 33 (1) (1980) 17–25, https://doi.org/10.1016/0022-4596(80)90543-5.

[35] K. Cao, R. Zheng, S. Wang, J. Shu, X. Liu, H. Liu, K.J. Huang, Q.S. Jing, L. Jiao, Boosting coulombic efficiency of conversion-reaction anodes for potassium-ion batteries via confinement effect, Adv. Funct. Mater. 30 (52) (2020) 2007712, https://doi.org/10.1002/adfm.202007712.

[36] T.X. Nguyen, Y.H. Su, C.C. Lin, J.M. Ting, Self-reconstruction of sulfate-containing high entropy sulfide for exceptionally high-performance oxygen evolution reaction electrocatalyst, Adv. Funct. Mater. 31 (48) (2021) 2106229, https://doi.org/10.1002/adfm.202106229.

[37] F. Sun, C. Wang, M. Osenberg, K. Dong, S. Zhang, C. Yang, Y. Wang, A. Hilger, J. Zhang, S. Dong, H. Markötter, I. Manke, G. Cui, Clarifying the electro-chemo-mechanical coupling in $Li_{10}SnP_2S_{12}$ based all-solid-state batteries, Adv. Energy Mater. 12 (13) (2022) 2103714, https://doi.org/10.1002/aenm.202103714.

[38] Y. Zhao, J. Zhu, S.J.H. Ong, Q. Yao, X. Shi, K. Hou, Z.J. Xu, L. Guan, High-rate and ultralong cycle-life potassium Ion batteries enabled by in situ engineering of yolk–shell FeS_2@C structure on graphene matrix, Adv. Energy Mater. 8 (36) (2018) 1802565, https://doi.org/10.1002/aenm.201802565.

[39] Y. Xu, J. Sun, Y. He, J. Li, J. Xu, Y. Sun, J. Liao, X. Zhou, Construction of CoS_2 nanoparticles embedded in well-structured carbon nanocubes for high-performance potassium-ion half/full batteries, Sci. China Chem. 64 (2021) 1401–1409, https://doi.org/10.1007/s11426-021-1057-3.

[40] J. Deng, X. Huang, M. Wang, M. Xu, Facile synthesis of Cu_2S nanoplates as anode for potassium ion batteries, Mater. Lett. 262 (2020), 127048, https://doi.org/10.1016/j.matlet.2019.127048.

[41] Z. Zhao, Z. Hu, R. Jiao, Z. Tang, P. Dong, Y. Li, S. Li, H. Li, Tailoring multi-layer architectured FeS_2@C hybrids for superior sodium-, potassium- and aluminum-ion storage, Energy Stor. Mater. 22 (2019) 228–234, https://doi.org/10.1016/j.ensm.2019.01.022.

[42] H. Gao, T. Zhou, Y. Zheng, Q. Zhang, Y. Liu, J. Chen, H. Liu, Z. Guo, CoS quantum dot nanoclusters for high-energy potassium-ion batteries, Adv. Funct. Mater. 27 (43) (2017) 1702634, https://doi.org/10.1002/adfm.201702634.

[43] L. Yang, W. Hong, Y. Zhang, Y. Tian, X. Gao, Y. Zhu, G. Zou, H. Hou, X. Ji, Hierarchical NiS_2 modified with bifunctional carbon for enhanced potassium-ion storage, Adv. Funct. Mater. 29 (50) (2019) 1903454, https://doi.org/10.1002/adfm.201903454.

[44] Q. Peng, S. Zhang, H. Yang, B. Sheng, R. Xu, Q. Wang, Y. Yu, Boosting potassium storage performance of the Cu_2S anode via morphology engineering and electrolyte

chemistry, ACS Nano 14 (5) (2020) 6024–6033, https://doi.org/10.1021/acsnano.0c01681.
[45] X. Li, H. Liang, B. Qin, M. Wang, Y. Zhang, H. Fan, Rational design of heterostructured bimetallic sulfides (CoS_2/NC@VS_4) with VS_4 nanodots decorated on CoS_2 dodecahedron for high-performance sodium and potassium ion batteries, J. Colloid Interface Sci. 625 (2022) 41–49, https://doi.org/10.1016/j.jcis.2022.05.155.
[46] J. Xie, Y. Zhu, N. Zhuang, H. Lei, W. Zhu, Y. Fu, M.S. Javed, J. Li, W. Mai, Rational design of metal organic framework-derived FeS_2 hollow nanocages@reduced graphene oxide for K-ion storage, Nanoscale 10 (36) (2018) 17092–17098, https://doi.org/10.1039/C8NR05239E.
[47] K. Kishi, J. Nishioka, Interaction of Fe/Cu(100), Fe-Ni/Cu(100) and Ni/Fe/Cu(100) surfaces with O_2 studied by XPS, Surf. Sci. 227 (1–2) (1990) 97–106, https://doi.org/10.1016/0039-6028(90)90396-P.
[48] N. Turner, A. Single, Determination of peak positions and areas from wide-scan XPS spectra, Surf. Interface Anal. 15 (3) (1990) 215–222, https://doi.org/10.1002/sia.740150305.
[49] I. Alstrup, I. Chorkendorff, R. Candia, B.S. Clausen, H. Topsøe, A combined X-Ray photoelectron and Mössbauer emission spectroscopy study of the state of cobalt in sulfided, supported, and unsupported Co Mo catalysts, J. Catal. 77 (2) (1982) 397–409, https://doi.org/10.1016/0021-9517(82)90181-6.
[50] L.-S. Hsu, R.S. Williams, Electronic-structure study of the Ni-Ga and the Ni-In intermetallic compounds using X-ray photoemission spectroscopy, J. Chem. Phys. 55 (4) (1994) 305–312, https://doi.org/10.1016/0022-3697(94)90226-7.
[51] O. Nishimura, K. Yabe, M. Iwaki, X-ray photoelectron spectroscopy studies of high-dose nitrogen ion implanted-chromium: a possibility of a standard material for chemical state analysis, J. Electron Spectrosc. Relat. Phenom. 49 (3) (1989) 335–342, https://doi.org/10.1016/0368-2048(89)85021-2.
[52] X.-R. Yu, F. Liu, Z.-Y. Wang, Y. Chen, Auger parameters for sulfur-containing compounds using a mixed aluminum-silver excitation source, J. Electron Spectrosc. Relat. Phenom. 50 (2) (1990) 159–166, https://doi.org/10.1016/0368-2048(90)87059-W.
[53] X. Liu, J.Q. Huang, Q. Zhang, L. Mai, Nanostructured metal oxides and sulfides for lithium–sulfur batteries, Adv. Mater. 29 (20) (2017) 1601759, https://doi.org/10.1002/adma.201601759.
[54] Q. Liu, W. Deng, C.-F. Sun, A potassium–tellurium battery, Energy Storage Mater. 28 (2020) 10–16, https://doi.org/10.1016/j.ensm.2020.02.021.
[55] Z. Zhao, Z. Yi, H. Li, R. Pathak, Z. Yang, X. Wang, Q. Qiao, Synergetic effect of spatially separated dual co-catalyst for accelerating multiple conversion reaction in advanced lithium sulfur batteries, Nano Energy 81 (2021), 105621, https://doi.org/10.1016/j.nanoen.2020.105621.
[56] J. Häcker, D.H. Nguyen, T. Rommel, Z. Zhao-Karger, N. Wagner, K.A. Friedrich, Operando UV/vis spectroscopy providing insights into the sulfur and polysulfide dissolution in magnesium–sulfur batteries, ACS Energy Lett. 7 (1) (2021) 1–9, https://doi.org/10.1021/acsenergylett.1c02152.
[57] H.-J. Yang, C.-Y. Chen, F.-W. Yuan, H.-Y. Tuan, Designed synthesis of solid and hollow $Cu_{2-x}Te$ nanocrystals with tunable near-infrared localized surface plasmon resonance, J. Phys. Chem. C. 117 (42) (2013) 21955–21964, https://doi.org/10.1021/jp407559b.
[58] X. Lu, M.E. Bowden, V.L. Sprenkle, J. Liu, A low cost, high energy density, and long cycle life potassium–sulfur battery for grid-scale energy storage, Adv. Mater. 27 (39) (2015) 5915–5922, https://doi.org/10.1002/adma.201502343.
[59] G. Janz, J. Coutts, J. Downey, E. Roduner, Raman studies of sulfur-containing anions in inorganic polysulfides. Potassium polysulfides, *Inorg.* 15 (8) (1976) 1755–1759, https://doi.org/10.1021/ic50162a003.
[60] Y.-Y. Hsieh, K.-T. Chen, H.-Y. Tuan, A synergetic SnSb-amorphous carbon composites prepared from polyesterification process as an ultrastable potassium-ion battery anode, Chem. Eng. J. 420 (2021), 130451, https://doi.org/10.1016/j.cej.2021.130451.
[61] Y.-Y. Hsieh, H.-Y. Tuan, Architectural van der Waals Bi_2S_3/Bi_2Se_3 topological heterostructure as a superior potassium-ion storage material, Energy Storage Mater. 51 (2022) 789–805, https://doi.org/10.1016/j.ensm.2022.07.020.
[62] S. Chong, L. Sun, C. Shu, S. Guo, Y. Liu, W.A. Wang, H.K. Liu, Chemical bonding boosts nano-rose-like MoS_2 anchored on reduced graphene oxide for superior potassium-ion storage, Nano Energy 63 (2019), 103868, https://doi.org/10.1016/j.nanoen.2019.103868.
[63] F. Wang, Y. Liu, H.-J. Wei, T.-F. Li, X.-H. Xiong, S.-Z. Wei, F.-Z. Ren, A.A. Volinsky, Recent advances and perspective in metal coordination materials-based electrode materials for potassium-ion batteries, Rare Met. 40 (2021) 448–470, https://doi.org/10.1007/s12598-020-01649-1.
[64] W.-C. Lin, Y.-C. Yang, H.-Y. Tuan, Ternary chalcogenide anodes for high-performance potassium-ion batteries and hybrid capacitors via composition-mediated bond softening and intermediate phase, Energy Storage Mater. 51 (2022) 38–53, https://doi.org/10.1016/j.ensm.2022.06.010.
[65] Y.-F. Huang, Y.-C. Yang, H.-Y. Tuan, Construction of strongly coupled few-layer $FePSe_3$-CNT hybrids for high performance potassium-ion storage devices, Chem. Eng. J. 451 (2023), 139013, https://doi.org/10.1016/j.cej.2022.139013.
[66] W. Zong, H. Guo, Y. Ouyang, L. Mo, C. Zhou, G. Chao, J. Hofkens, Y. Xu, W. Wang, Y.-E. Miao, G. He, I.P. Parkin, F. Lai, T. Liu, Topochemistry-driven synthesis of transition-metal selenides with weakened Van Der Waals Force to enable 3D-printed Na-ion hybrid capacitors, Adv. Funct. Mater. 32 (13) (2022) 2110016, https://doi.org/10.1002/adfm.202110016.
[67] J. Ge, B. Wang, J. Wang, Q. Zhang, B. Lu, Nature of $FeSe_2$/N-C anode for high performance potassium ion hybrid capacitor, Adv. Energy Mater. 10 (4) (2020) 1903277, https://doi.org/10.1002/aenm.201903277.